Multifrequency and Multimodal Sparse Reconstruction in Lamb Wave Based Structural Health Monitoring

Andrew Golato, Sridhar Santhanam*, Fauzia Ahmad, Moeness G. Amin
Center for Advanced Communications, College of Engineering, Villanova University,
800 E. Lancaster Ave., Villanova, PA 19085, USA.

ABSTRACT

In structural health monitoring, Lamb waves are employed extensively to examine and monitor thin structures, such as plates and shells. Typically, a network of piezoelectric transducers is attached to the structural plate member and used for both transmission and reception of the Lamb waves. The signals scattered from defects in the plate are recorded by employing the transducers in pitch-catch pairings. In this paper, we propose a multifrequency, multi-modal sparse reconstruction approach for localizing defects in thin plates. We simultaneously invert Lamb wave based scattering models for both fundamental propagating symmetric and anti-symmetric wave modes, while exploiting the inherent sparsity of the defects. Dictionaries are constructed for both fundamental wave modes, which account for associated dispersion and attenuation as a function of frequency. Signals are collected at two independent frequencies; one at which the fundamental symmetric mode is dominant, and the other at which only the fundamental anti-symmetric wave mode is present. This provides distinct and separable multi-modal contributions, thereby permitting sparse reconstruction of the region of interest under the multiple measurement vector framework. The proposed defect localization approach is validated using simulated data for an aluminum plate.

Keywords: Sparse reconstruction, multimodal, dual frequency, Lamb waves, compressed sensing, structural health monitoring

1. INTRODUCTION

Today, Structural Health Monitoring (SHM) has emerged as a leading technology in the assessment of the integrity or health of a structure.[1-4] With applications to a variety of structures, and associated self-sensing capabilities of the structures, much of the recent attention has been given to this field. Under the umbrella of SHM, guided ultrasonic waves find favor in the real-time imaging of defects in thin-walled structures, which include airplanes, bridges, and windmills. The utilization of a self-sensing, real-time system in such structures fosters safety and offers economic advantages.[5-6]

Lamb waves have gained preference in the SHM of thin-walled structures. These guided waves, unique to thin plates and shell structures, can travel large distances without significant attenuation, while also lending themselves to rich interactions with defects.[7-9] Propagation characteristics of Lamb waves can be obtained by solving the wave equation for a thin plate with traction free surface conditions.[10,11] These waves are multimodal in nature, and can be separated into symmetric (S) and anti-symmetric (A) modes. While, in general, there are an infinite number of symmetric and anti-symmetric modes, the number of such modes present in a structure can be regulated by the frequency of excitation in relation to the thickness of the plate. At higher frequencies, an overabundance of wave modes exist, while at lower frequencies, only the fundamental S_0 and A_0 modes are present.

Typically, in order to induce these waves in a structure, a network of piezoelectric (PZT: Lead Zirconate Titanate) transducers is attached to the surface. Windowed sinusoidal pulses excite the transmitting transducers, thereby inciting Lamb waves in the structure. These waves travel through the structure, interact with any defects present, and arrive at the receiving transducers in the network. While the frequency of excitation regulates the wave modes present in the structure, the choice of transducer size will also affect the relative strength or amplitude of the individual wave mode packets.[12] Hence, the propagating wave can be reduced to a single dominant symmetric or anti-symmetric mode through the appropriate choice of transducer and excitation frequency.

While these choices can lend predictability to the received signal, the dependence of the phase and group velocities of the individual modes on frequency will complicate the signal. Frequency-dependent velocities change the shape of the waves during propagation via dispersion. Additional reflections by the boundaries or edges of the structure can further

*sridhar.santhanam@villanova.edu; http://www1.villanova.edu/villanova/engineering/research/centers/cac/facilities/aul.html

complicate the guided Lamb wave signal.[5-6,13] Despite the complexities, exploitation of the information contained in the various modes provides an enhanced assessment of the health of the structure. For example, the S_0 mode is well-suited at detecting transverse cracks in the middle of plates, while the A_0 mode interacts best with delamination cracks lying in a plane parallel to the plane of the plate.[14]

Once the scattered signal is received, processing is necessary in order to extract the desired information. Most often, the first step in processing involves the subtraction of a baseline signal (signal received with no defect present) from the received signal, thereby producing a residual signal primarily displaying the effects of the defects.[5-6] This step is followed by an image formation process whereby the scene (area under investigation) is reconstructed. While both data-independent and adaptive beamforming approaches have been employed in the past for scene reconstruction in order to detect the presence of defects, none of these methods exploit the sparsity of scattering sources (defects) in the structure for image recovery.[15-16] In recent work, the defect imaging problem in Lamb wave based SHM was cast in a sparse reconstruction framework by recognizing that the number of defects is typically small.[5-6] Reasonably accurate imaging results with sufficient resolution of neighboring defects in the presence of noise were obtained via an l_1-norm minimization approach. While this work found success, the multimodal nature of Lamb waves was not exploited.

More recently, a multimodal scene reconstruction approach for localizing defects in thin plates has been proposed by the authors.[17] This approach inverts a multimodal Lamb wave based model through exploitation of the sparsity of the defects. It considers both symmetric and anti-symmetric fundamental propagating Lamb modes and constructs model-based dictionaries for each mode, taking into account the associated dispersion and attenuation through the medium. Image recovery is performed jointly across the two modes using the group sparsity constraint.[17-21] While this method provides good results, it does not take advantage of the separability of the modes and associated signals, which is offered by excitation of the individual modes at distinct frequencies as considered in this paper. In the current work, using two unique transducer-frequency combinations, model-based dictionaries are constructed and utilized, in conjunction with a mode-separable signal, to reconstruct the image jointly across the two modes within the multiple measurement vector framework. The effectiveness of the proposed method is demonstrated using simulated data for an aluminum plate.

The remainder of the paper is organized as follows. In Section 2, we describe the signal propagation model and present the sparse reconstruction algorithm for exploitation of the multifrequency-multimodal propagating Lamb modes. Results based on simulated data are discussed in Section 3. Section 4 contains the concluding remarks.

2. MULTIMODAL SIGNAL MODEL AND SPARSE RECONSTRUCTION

A spatially distributed network of *J* transducers is considered. Each sensor can both transmit and receive signals in the form of Lamb waves. The transducers are employed for data collection in pairs, in a pitch-catch mode. For *J* transducers, a total of $L = J!/(J-2)!$ transmit-receive pairs are used.

Consider the lth transmit-receive pair, with the transmitter and receiver located at position vectors $\boldsymbol{t}_l$ and $\boldsymbol{r}_l$, respectively. The transmitter is excited by a waveform $h(t)$, whose center frequency is carefully chosen to match the transducer such that only a single mode (either the fundamental A_0 mode, analyzed at center frequency f_{A_0}, or fundamental S_0 mode, analyzed at center frequency f_{S_0}) is produced. The direct propagation between the transmitter and the receiver in the absence of any defects is considered first. Let Λ denote either the propagating A_0 or S_0 mode, depending on the frequency of operation. The direct received signal, $G_{l,\Lambda}^{dir}(\cdot)$, can be expressed in the frequency domain as

$$G_{l,\Lambda}^{dir}(f) = (\alpha_l/\|\boldsymbol{t}_l - \boldsymbol{r}_l\|_2)^{0.5} H(f) \exp(j\, 2\pi f \|\boldsymbol{t}_l - \boldsymbol{r}_l\|_2 / c_\Lambda(f)), \tag{1}$$

where $H(f)$ is the Fourier transform of $h(t)$, c_Λ is the frequency-dependent phase speed for the mode Λ, α_l is a normalizing constant for the distance of the lth transmit-receive pair. The attenuation caused by the geometrical spreading of the circular wavefront is captured by the inverse square root dependence on $\|\boldsymbol{t}_l - \boldsymbol{r}_l\|_2$. The time-domain equivalents of the A_0 and S_0 signals, $g_{l,A_0}^{dir}(t)$ and $g_{l,S_0}^{dir}(t)$, are the inverse Fourier transforms of equation (1) for $\Lambda = A_0$ and S_0, respectively. Thus, the baseline signal corresponding to the lth transmit-receive pair for the Λ mode is given by

$$z_{l,\Lambda}^{dir}(t) = g_{l,\Lambda}^{dir}(t), \tag{2}$$

It is noted that, in addition to the direct signal, the received signal may contain scattering from the boundaries of the plate. These additional contributions, however, are quite weak provided that the plate boundaries are sufficiently far away from the area being interrogated. As such, they are not included in the baseline signal in eq. (2).

Next, consider a defect located at position vector $\boldsymbol{s}_p$. In addition to the direct propagation of the Λ mode, signals scattered by the defect arrive at the receiver. If the defect is symmetric, the scattered signal will consist of a single mode, the Λ mode. On the other hand, asymmetric defects can spawn additional scattered modes. As a result, the scattered signal can contain both fundamental modes. It is assumed here that the dominant scattered mode is the Λ mode. The received scattered wave in the frequency domain for the Λ mode is given by,

$$G_{lp,\Lambda}^{sc}(f) = \left(\frac{\beta_{lp}}{\|\boldsymbol{t}_l - \boldsymbol{s}_p\|_2}\right)^{0.5} \left(\frac{\gamma_{lp}}{\|\boldsymbol{r}_l - \boldsymbol{s}_p\|_2}\right)^{0.5} S_{p,\Lambda}(f, \theta_{l,in}, \theta_{l,out})\, H(f)\, \exp\left(j2\pi f(\|\boldsymbol{t}_l - \boldsymbol{s}_p\|_2 + \|\boldsymbol{r}_l - \boldsymbol{s}_p\|_2)/c_\Lambda(f)\right), \quad (3)$$

where β_{lp} and γ_{lp} are the respective normalizing constants for the distances of the *l*th transmitter and receiver to the *p*th defect, $S_{p,\Lambda}$ is the frequency-domain defect response for the Λ mode, which is typically a function of frequency, the incident angle $\theta_{l,in}$ and the scattered angle $\theta_{l,out}$. The equivalent time-domain version, $g_{lp,\Lambda}^{sc}(t)$, is the respective inverse Fourier transform of eq. (3) for mode Λ . In the presence of the defect at $\boldsymbol{s}_p$, the total received signal at $\boldsymbol{r}_l$ is the sum of the direct and scattered signal components corresponding to the Λ mode,

$$z_{l,\Lambda}(t) = g_{l,\Lambda}^{dir}(t) + g_{lp,\Lambda}^{sc}(t). \quad (4)$$

For the case of *P* structural defects in the plate, the total received signal, corresponding to the *l*th transmit-receive pair, is the superposition of the direct signal and the scattered modes produced by all defects, which can be expressed as

$$z_{l,\Lambda}(t) = g_{l,\Lambda}^{dir}(t) + \sum_{p=0}^{P-1}\left(g_{lp,\Lambda}^{sc}(t)\right). \quad (5)$$

Note that the interactions between the defects are ignored in this model. Background subtraction is applied as follows,

$$\delta z_{l,\Lambda} = z_{l,\Lambda}(t) - z_{l,\Lambda}^{dir}(t) = \sum_{p=0}^{P-1}\left(g_{lp,\Lambda}^{sc}(t)\right). \quad (6)$$

The *l*th difference signal, $\delta z_{l,\Lambda}$, contains only the scattered signal components for mode Λ. The direct components are the same over the two measurements and are, thus, removed from the difference signal.

2.2 Multimodal Linear Signal Model

Consider the special case of angle- and frequency-independent defect scattering responses, i.e. $S_{p,\mathrm{A}_0}(f, \theta_{l,in}, \theta_{l,out}) = x_{p,\mathrm{A}_0}$ and $S_{p,\mathrm{S}_0}(f, \theta_{l,in}, \theta_{l,out}) = x_{p,\mathrm{S}_0}, \forall\, f, l.$ Future work will consider the more general case of frequency- and angle-dependent scattering responses.

The equivalent matrix-vector representation of the difference signals, $\delta z_{l,\Lambda}, l = 0,1,\cdots,L-1$, corresponding to mode Λ, is obtained as follows. The area under investigation, or region of interest (ROI) is conceptualized as a uniform grid of *M* points representing the potential defect locations. *M* is assumed to be much greater than *P*, which corresponds to the sparsity assumption that most of the area is assumed to be defect-free. Let $\boldsymbol{x}_{\mathrm{A}_0}$ and $\boldsymbol{x}_{\mathrm{S}_0}$ be the concatenated $M \times 1$ scene reflectivity vectors corresponding to the spatial sampling grid under the A_0 and S_0 modes, respectively. Vectors $\boldsymbol{x}_{\mathrm{A}_0}$ and $\boldsymbol{x}_{\mathrm{S}_0}$ are the outputs of weighted indicator functions. If the *p*th defect exists at the *m*th grid-point, the element *m* of these vectors takes the values x_{p,A_0} and x_{p,S_0}, respectively; otherwise, the element *m* is equal to zero. The *l*th difference signal, $\delta z_{l,\Lambda}$, is sampled at times $t_k, k = 0,1,\cdots,K-1$, to obtain a $K \times 1$ vector $\Delta \boldsymbol{z}_l$. Then, using equations (3) and (6), we obtain the relationship between the *l*th difference signal for mode Λ and the corresponding scene reflectivity vector as

$$\Delta \boldsymbol{z}_{l,\mathrm{A}_0} = \boldsymbol{\Psi}_{l,\mathrm{A}_0} \boldsymbol{x}_{\mathrm{A}_0}, \quad (7)$$

$$\Delta \boldsymbol{z}_{l,\mathrm{S}_0} = \boldsymbol{\Psi}_{l,\mathrm{S}_0} \boldsymbol{x}_{\mathrm{S}_0}, \quad (8)$$

where $\boldsymbol{\Psi}_{l,\mathrm{A}_0}$ and $\boldsymbol{\Psi}_{l,\mathrm{S}_0}$ are dictionary matrices of dimensions $K \times M$. The *m*th column of $\boldsymbol{\Psi}_{l,\mathrm{A}_0}$ consists of the scattered A_0 wave at the center frequency f_{A_0}, corresponding to a defect at the *m*th grid-point $\boldsymbol{s}_m$, and the *k*th element of the *m*th column can be written as

$$\left[\boldsymbol{\Psi}_{l,\mathrm{A}_0}\right]_{k,m} = \mathcal{F}^{-1}\left\{\left(\frac{\beta_{lp}}{\|\boldsymbol{t}_l-\boldsymbol{s}_m\|_2}\right)^{0.5}\left(\frac{\gamma_{lp}}{\|\boldsymbol{r}_l-\boldsymbol{s}_m\|_2}\right)^{0.5} H(f)\ \exp\left(j2\pi f(\|\boldsymbol{t}_l-\boldsymbol{s}_m\|_2+\|\boldsymbol{r}_l-\boldsymbol{s}_m\|_2)/c_{\mathrm{A}_0}(f)\right)\right\}\Big|_{t=t_k}. \quad (9)$$

Likewise, the *m*th column of $\boldsymbol{\Psi}_{l,\mathrm{S}_0}$ consists of the scattered S_0 wave at the center frequency f_{S_0}, corresponding to a defect at $\boldsymbol{s}_m$ with its *k*th element given by

$$\left[\boldsymbol{\Psi}_{l,\mathrm{S}_0}\right]_{k,m} = \mathcal{F}^{-1}\left\{\left(\frac{\beta_{lp}}{\|\boldsymbol{t}_l-\boldsymbol{s}_m\|_2}\right)^{0.5}\left(\frac{\gamma_{lp}}{\|\boldsymbol{r}_l-\boldsymbol{s}_m\|_2}\right)^{0.5} H(f)\ \exp\left(j2\pi f(\|\boldsymbol{t}_l-\boldsymbol{s}_m\|_2+\|\boldsymbol{r}_l-\boldsymbol{s}_m\|_2)/c_{\mathrm{S}_0}(f)\right)\right\}\Big|_{t=t_k}. \quad (10)$$

Equations (7) and (8) consider the contribution of only one transmit-receive pair. For each mode, stacking the difference signal vectors corresponding to all L pairs allows the formation of the $KL \times 1$ vector:

$$\Delta\boldsymbol{z}_\Lambda = \left[\Delta\boldsymbol{z}_{0,\Lambda}^T \quad \Delta\boldsymbol{z}_{1,\Lambda}^T \quad \cdots \quad \Delta\boldsymbol{z}_{L-1,\Lambda}^T\right]^T, \quad (11)$$

where the superscript 'T' denotes the matrix transpose operation. Eqs. (7), (8), and (11) together yield the linear system of equations

$$\Delta\boldsymbol{z}_{\mathrm{A}_0} = \boldsymbol{\Psi}_{\mathrm{A}_0}\boldsymbol{x}_{\mathrm{A}_0}, \quad (12)$$

$$\Delta\boldsymbol{z}_{\mathrm{S}_0} = \boldsymbol{\Psi}_{\mathrm{S}_0}\boldsymbol{x}_{\mathrm{S}_0}, \quad (13)$$

where

$$\boldsymbol{\Psi}_\Lambda = \left[\boldsymbol{\Psi}_{0,\Lambda}^T\ \boldsymbol{\Psi}_{1,\Lambda}^T\ \cdots\ \boldsymbol{\Psi}_{L-1,\Lambda}^T\right]^T, \text{ for } \Lambda = \mathrm{A}_0, \mathrm{S}_0. \quad (14)$$

denote the respective dictionaries of size $KL \times M$ corresponding to the A_0 and S_0 propagation modes at the center frequencies f_{A_0} and f_{S_0}, respectively.

2.3 Multifrequency Block Diagonal Group Sparse Reconstruction

Signal propagation and reception occur independently at the two distinct frequencies (f_{A_0} and f_{S_0}) for the two modes. It is assumed here that the reflectivity of the defects will depend on the nature of the fundamental mode (A_0 or S_0) that is incident upon it. Therefore, no prior knowledge of the exact relationship between $\boldsymbol{x}_{\mathrm{A}_0}$ and $\boldsymbol{x}_{\mathrm{S}_0}$ can be assumed. Nevertheless, it is clear that both reflectivity vectors represent the same scene. Hence, they share a common support. That is, if a particular element of $\boldsymbol{x}_{\mathrm{A}_0}$ is nonzero, then so should be the corresponding element of $\boldsymbol{x}_{\mathrm{S}_0}$. This correlation lends itself to a group sparse reconstruction. Furthermore, the resolvability of the distinct A_0 and S_0 components of the received signal, by virtue of operation at two separate frequencies, permits a block diagonal structure to be utilized for group reconstruction, as described next.

The separable modal contributions $\Delta\boldsymbol{z}_\Lambda$ are stacked into a tall vector $\Delta\boldsymbol{z} = [\Delta\boldsymbol{z}_{\mathrm{A}_0}^T\ \Delta\boldsymbol{z}_{\mathrm{S}_0}^T]^T$. A stacked signal model is formed from equations (12) and (13) as

$$\Delta\boldsymbol{z} = \boldsymbol{\Psi}\boldsymbol{x}, \quad (15)$$

with a stacked scene reflectivity vector $\boldsymbol{x} = [\boldsymbol{x}_{\mathrm{A}_0}^T\ \boldsymbol{x}_{\mathrm{S}_0}^T]^T$ and a combined multimodal dictionary, $\boldsymbol{\Psi} = \boldsymbol{bdiag}\left(\boldsymbol{\Psi}_{\mathrm{A}_0}, \boldsymbol{\Psi}_{\mathrm{S}_0}\right) = \begin{pmatrix}\boldsymbol{\Psi}_{\mathrm{A}_0} & \mathbf{0}\\ \mathbf{0} & \boldsymbol{\Psi}_{\mathrm{S}_0}\end{pmatrix}$, where $\mathbf{0}$ represents a zero matrix of size $KL \times M$.

Owing to the aforementioned group sparse nature of the problem at hand, the nonzero values in $\boldsymbol{x}$ will appear in groups of length two rather than being arbitrarily spread throughout the stacked vector. The group-sparse vector $\boldsymbol{x}$ can be recovered from the measurements $\Delta\boldsymbol{z}$ in equation (15) through a mixed l_2/l_1 norm optimization[18] or a block version of the Orthogonal Matching Pursuit algorithm (BOMP)[19]. The latter will be utilized in this work for scene recovery. Once the stacked vector has been reconstructed, the recovered vectors $\hat{\boldsymbol{x}}_{\mathrm{A}_0}$ and $\hat{\boldsymbol{x}}_{\mathrm{S}_0}$ are combined to obtain a single composite scene representation $\tilde{\boldsymbol{x}}$. This is achieved by calculating the l_2 norm across the elements of these vectors as[17]

$$[\tilde{\boldsymbol{x}}]_m = \tilde{x}_m = \left\|[\hat{x}_{m,\mathrm{A}_0} \quad \hat{x}_{m,\mathrm{S}_0}]^T\right\|_{\mathbf{2}}. \quad (16)$$

3. SIMULATION RESULTS

Consider a network of ten transducers (A, B, C, D, and E; and A',B',C',D', and E') located circumferentially around a circle of radius 250mm, centered at the center of a 1.22m square plate. The transducer coordinates are specified in Table 1 and the geometry is presented in Fig.2. The prime (') denotes transducers that generate the S_0 wave mode (depicted as larger green circles in Fig. 2); non-primed transducers (represented by smaller red circles in the Fig. 2) have an A_0 modal bias. The ROI is a 400mm by 400mm square centered at the center of the plate, as shown by the cyan mesh-grid in Fig. 2. All coordinates are relative to the origin, denoted by the blue circle in Fig. 2 in the lower left-hand corner of the 500 mm square that perfectly circumscribes the transducer circle.

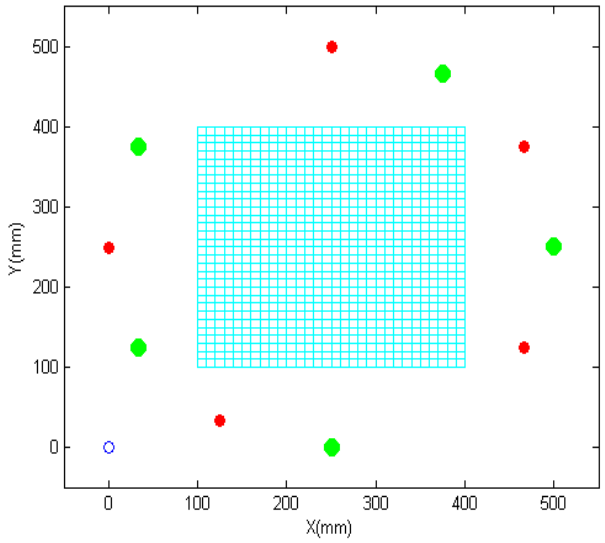

Figure 1. Schematic of the simulation setup. Only the part of the plate containing the transducers and the defects is shown.

PZT	X(mm)	Y(mm)		PZT	X(mm)	Y(mm)
A	250	500		A'	375	467
B	467	375		B'	500	250
C	467	125		C'	250	0
D	125	34		D'	34	125
E	0	250		E'	34	375

Table 1. Transducer locations, X-Y coordinates in millimeters.

For each mode, there are five transducers resulting in 20 transmit-receive pairings. However, it is understood that for the case of a single wave mode propagating from the transmitter to the receiver, the path from A to B is identical to the path from B to A; therefore, we can eliminate the double counts, i.e. we consider $L = 10$ distinct combinations for each mode. The excitation is chosen to be a Hanning-windowed, five-cycle burst of a sinusoidal signal. For A_0 mode, the sinusoidal burst was centered at 100 kHz and generated using the non-prime transducers. For the S_0 mode, the center frequency was selected to be 175 kHz using the primed transducers. The choice of using separate transducers reflects experimental constraints by which separate and different transducers must be utilized in order to isolate solitary wave modes[12]. The corresponding phase velocities, c_{A_0} and c_{S_0}, for the A_0 and S_0 modes are frequency dependent; therefore,

dispersion is accounted for in the dictionary matrices. The ROI is divided into 31 × 31 ($M = 961$) grid points. Two defects are introduced to the scene and modeled as point scatterers with modal bias, i.e. they will scatter either the A_0 mode or the S_0 mode, but not both. The first defect is located at (160,160) mm, and it reflects S_0, such that $x_{0,S_0} = 1$, while $x_{0,A_0} = 0.0$. The second defect, located at (340,340) mm, produces a strong A_0 mode, with $x_{1,A_0} = 1$, while not reflecting the S_0 mode ($x_{1,S_0} = 0.0$.) The scattered signal corresponding to each transmit-receive pair is sampled at 1 MHz for each mode and consists of $K = 1024$ time samples; thus, the total number of samples for all ten transmit-receive pairs is 10240 for each mode. Therefore, the length of $\Delta \boldsymbol{z}$ in equation (15) is 20480 samples. White Gaussian noise was added with -20 dB signal-to-noise ratio (SNR) to the simulated signal measurements. The individual modal dictionaries, $\boldsymbol{\Psi}_{A_0}$ and $\boldsymbol{\Psi}_{S_0}$, corresponding to the individual A_0 and S_0 modes, are of size 10240 × 961 each; thus, the block-diagonal multimodal dictionary $\boldsymbol{\Psi}$ of equation (15) has the dimensions 20480 × 1922.

First, consider the single-mode based sparse scene recovery in which $\boldsymbol{\Psi}_{S_0}$ and $\boldsymbol{\Psi}_{A_0}$ are utilized individually and independently. Orthogonal matching pursuit[21] (OMP) is used to reconstruct the sparse vector $\boldsymbol{x}_{A_0}$ by only considering the linear signal model of equations (12), while $\boldsymbol{x}_{S_0}$ is reconstructed using OMP and the signal model in equation (13). For the reconstruction, the number of OMP iterations was set to 2 in each case; hence, the single-mode reconstructions operate under an over-specified sparsity parameter, sine only a single defect can be seen by a specific mode. Figs. 3(a) and 3(b) depict the single-mode sparse reconstruction results for the A_0 and S_0 modes, respectively. Since one defect preferentially reflects A_0 mode and the other defect biases the S_0 mode, each single mode reconstruction predictably only identifies one of the two true targets, while placing its other selection at a false position.

Instead of the joint reconstruction of the two reflectivity vectors under the group sparsity framework, we first consider averaging the intensities of the independent single-mode reconstructions to yield the composite reconstructed scene image, shown in Fig. 4(a). In so doing, both true defect locations are identified; however, two additional false selections are also present. Next, we utilize the group sparse reconstruction using BOMP with 2 iterations. The group sparse result, is displayed in Fig. 4(b). It is clear from Fig. 4(b) that the proposed multimodal, multifrequency group sparse reconstruction approach provides superior performance in high noise scenarios, as it correctly detects and localizes both defects without introducing any false alarms.

In order to quantify the performance of the multimodal-multifrequency approach over single-mode reconstructions, we use the Earth Movers Distance (EMD)[23-24] metric, which calculates the power necessary to transform the reconstructed image into the ground truth image. For the simulations, consider the same two defect scenario as above, with the same modal biases. The simulation is averaged over 100 Monte Carlo runs. The averaged mean and standard deviation of the EMD are plotted versus the SNR in Fig. 5 for the single mode only reconstructions only, the multimodal reconstruction

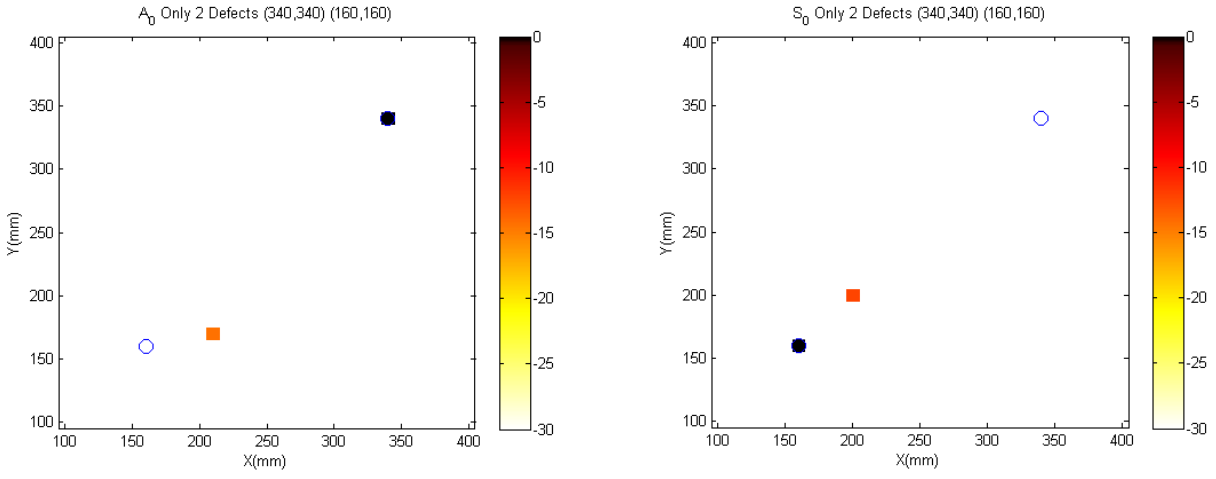

(a) (b)

Figure 3. Single-mode sparse reconstruction results using the (a) A_0 mode dictionary only, and (b) the S_0 mode dictionary only.

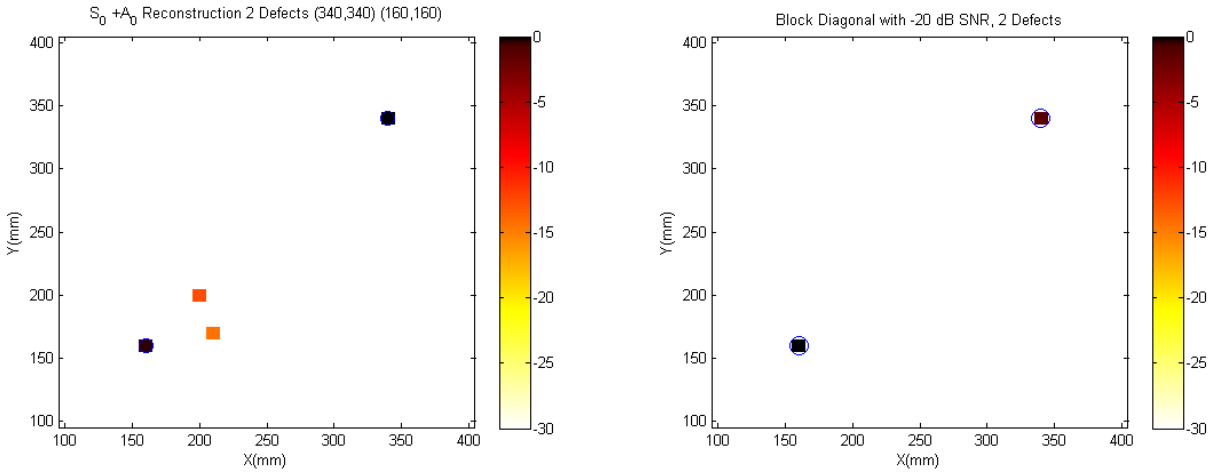

(a) (b)

Figure 4. Multimodal sparse reconstruction results using the (a) the intensity average of the A_0 only with the S_0 only result, and (b) the group sparse appraoch based on the multimodal multifrequency dictionary.

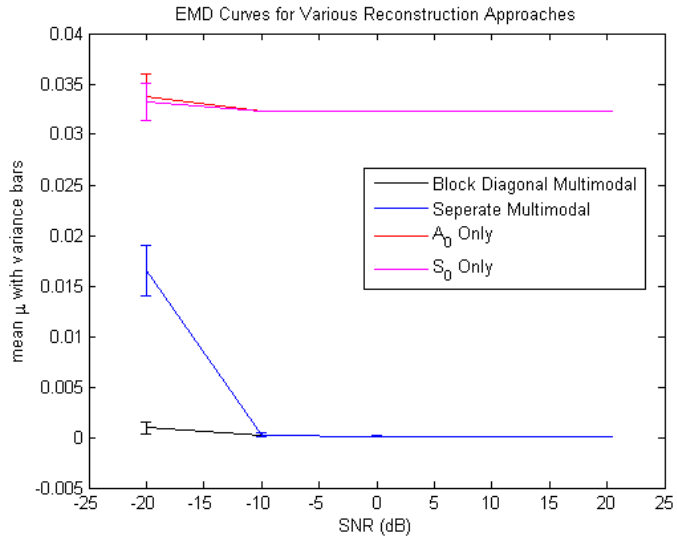

Figure 5. Plots of the mean and standard deviation of the EMD for the two single and two multimodal approaches. Reconstructions more closing matchign the ground truth obtain EMD values closer to zero.

obtained via the intensity average of the two single-mode reconstructions, and the group sparse reconstruction. For the Monte Carlo runs, SNR values in the [-20 20] dB range were considered with 10 dB increments. For all considered cases, both the mean value and the standard deviation of the EMD predictably decrease as SNR increases. However, it is noted that only when considering both modes does the EMD curve approach a zero mean value with a small standard deviation. This validates the superior performance of a multimodal approach over a single mode reconstruction. Furthermore, when considering unfavorable SNR conditions (-15dB and below), a clear advantage is seen in the block diagonal group approach.

Through these simulations, the shortcoming of a single-mode reconstruction is highlighted in case of biased defects. It is well known that different defects interact differently with each of the fundamental modes[9]. Hence, reconstruction based only on a single mode may fail to detect and localize all defects, assuming the bias of the defects is unknown. Since prior knowledge of the defect type present in the structure being interrogated is not typically available, an accurate and robust reconstruction is ensured by exploiting the multimodal nature of Lamb waves.

4. CONCLUSION

This paper proposed a sparse reconstruction approach, which exploits both the symmetric and anti-symmetric fundamental Lamb modes in order to identify and localize defects in thin plates. Two separate excitation frequencies are employed to ensure resolvability of the multimodal scattered signals. Model-based dictionaries are constructed for each mode, whereby one dictionary considers an S_0 biased frequency and the other a separate frequency at which A_0 mode is more dominant. These dictionaries incorporate the associated dispersion and attenuation through the medium. Using these dictionaries, sparse reconstruction of the area being interrogated is performed jointly across the two modes using the notion of group sparsity, and by exploiting the block diagonal structure of the combined dictionary, which naturally arises in the multifrequency approach. Simulations for a thin aluminum plate are used to demonstrate the superior performance of the multimodal approach over the single-mode sparse reconstruction. Current pursuits involve experimental verification of the proposed multimodal multifrequency reconstruction approach.

ACKNOWLEDGMENT

This research was supported in part by the National Science Foundation (NSF) under grant number IIP-0917690.

REFERENCES

[1] Kessler, S. S., Spearing, S. M. and Soutis, C., "Structural health monitoring in composite materials using Lamb wave methods," *Smart Materials and Structures* 11(2), 269-278 (2002).

[2] Raghavan, A. and Cesnik, C. E. S., "A review of guided wave structural health monitoring," *Shock and Vibrations Digest* 39(2), 91-114 (2007).

[3] Giurgiutiu, V. and Santoni-Bottai, G., "Structural health monitoring of composite structures with piezoelectric wafer active sensors," *AIAA Journal* 49(3), 565-581 (2011).

[4] Santhanam, S. and Demirli, R., "Reflection and transmission of fundamental Lamb wave modes obliquely incident on a crack in a plate," *Proc. IEEE Int. Ultrasonics Symp.*, 2690-2693 (2012).

[5] Levine, R. M. and Michaels, R. M., "Model-based imaging of damage with Lamb waves via sparse reconstruction," *J. Acoust. Soc. Am.* 133(3), 1525-1534 (2013).

[6] Levine, R. M. and Michaels, J. E., "Block-Sparse Reconstruction and Imaging for Lamb Wave Structural Health Monitoring," *IEEE Trans. Ultrason., Ferroelectr., Freq. Control*, 61, 1006-1015(2014).

[7] Ramadas, C., Balasubramaniam, K., Joshi, M., and Krishnamurthy, C., "Interaction of the primary antisymmetric Lamb mode with the symmetric delaminations: numerical and experimental studies," *Smart Mater. Struct.* 18(1), 1-7 (2009).

[8] Sohn, H., Park, G., Walt, J., Limback, N. P. and Farrar, C., "Wavelet based active sensing for delamination detection in composite structures," *Smart Mater. Struct.* 13(1), 153-160 (2004).

[9] Tua, P., Quek, S. and Wang, Q., "Detection of cracks in plates using piezo-actuated Lamb waves," *Smart Mater. Struct.* 13(1), 643-660 (2004).

[10] Achenbach, J., [Wave Propagation in Elastic Solids], North Holland, New York (1984).

[11] Rose, J., [Ultrasonic Waves in Solid Media], Cambridge University Press, Cambridge, UK (1999).

[12] Giurgiutiu, V. "Tuned Lamb wave excitation and detection with piezoelectric wafer active sensors for structural health monitoring**,"** *J. Intel. Mat. Syst. Str.* 16 (4), 291-305 (2005).

[13] Santhanam, S. and Demirli, R., "Reflection of Lamb waves obliquely incident on the free edge of a plate," *Ultrasonics* 53(1), 271-282 (2013).

[14] Ng, C. and Veidt, M., "Scattering of the fundamental antisymmetric Lamb wave at delaminations in composite laminates," *J. Acoust. Soc. Am.* 129(1), 1288-1296 (2011).

[15] Johnson, D. H. and Dudgeon, D. E., [Array Signal Processing: Concepts and Techniques], Prentice Hall, (1993).

[16] Hall, J. and Michaels, J., "Minimum variance ultrasonic imaging applied to an in situ sparse guided wave array," *IEEE Trans. Ultrason., Ferroelectr., Freq. Control* 57 (10), 2311-2323 (2010).

[17] Golato, A., Santhanam,S., Ahmad,F., Amin, M., "Multimodal sparse reconstruction in Lamb wave-based structural health monitoring", Proc.of SPIE Vol. 9109, 91090P (2014)

[18] Yuan, M. and Lin, Y., "Model selection and estimation in regression with grouped variables," J. *Royal Stat. Soc. Series B* 68(1), 49–67 (2007).
[19] Eldar, Y. C., Kuppinger, P. and Bolcskei, H., "Block-sparse signals: Uncertainty relations and efficient recovery," *IEEE Trans. Signal Process*. 58(6), 3042–3054 (2010).
[20] Leigsnering, M., Ahmad, F., Amin, M. and Zoubir, A., "Compressive sensing based specular multipath exploitation for through-the-wall radar imaging," *Proc. IEEE Int. Conf. Acoust., Speech, Signal Process.*, 6004-6008 (2013).
[21] Amin, M. G. and Ahmad, F., "Compressive sensing for through-the-wall radar imaging," *J. Electron. Imaging.* 22(3), 030901 (2013).
[22] Tropp, J.A., "Greed is good: algorithmic results for sparse approximation," *IEEE Trans. Inf. Theory*. 50(10), 2231-2242 (2004).
[23] Rubner,Y., "Perceptual Metrics for Image Database Navigation," Ph.D. thesis, Stanford University, USA, 1999.
[24] Pele, O. and Werman, M., "Fast and robust earth mover's distances," Proc. IEEE 12th Int. Conf. Computer Vision, 460–467(2009).